Multi scale diffeomorphic metric mapping of spatial transcriptomics datasets

Michael I. Miller
Johns Hopkins University Department of Biomedical Engineering
Baltimore, MD, USA
mim@jhu.edu

Jean Fan
Johns Hopkins University Department of Biomedical Engineering
Baltimore, MD, USA
jeanfan@jhu.edu

Daniel J. Tward
University of California Los Angeles, Departments of Computational Medicine and Neurology
Los Angeles, CA, USA
dtward@mednet.ucla.edu

Abstract

Spatially resolved transcriptomic imaging is a family of promising new technologies that can produce a series of images that quantify gene expression at every pixel. These technologies, such as multiplex error-robust fluorescence in situ hybridization (MERFISH) which is the focus of this work, produce data that is inherently multi scale. They describe molecules at nanometer resolution, cell types at micron resolution, and tissue types at millimeter resolution. To harness the potential of these techniques, new mathematical and computational tools are required to quantify similarities and differences between images across experimental conditions. In this work we demonstrate the application of multi scale diffeomorphic metric mapping to MERFISH images. This recently developed framework uses varifold measures on reproducing kernel Hilbert spaces to describe shape and signal across spatial scales, and computes distances between samples in a Riemannian setting. Using experimental data from serial sections of the mouse preoptic hypothalamus, we use this technique to compute optimal nonrigid alignments between neighboring sections. This approach will ultimately be extended to 3D reconstruction and alignment to common coordinates of a brain atlas.

1. Introduction

Neuroimage analysis is a field that has strongly benefitted from computer vision techniques. Stereology practices including cell detection and tissue-type annotation that were once performed manually [24] are now being replaced by automatic methods. Many such tools rely on the Riemannian structure of shape data, such as the Large Deformation Diffeomorphic Metric Mapping (LDDMM) [2] framework upon which our work is built. This framework has been leveraged by many groups to study and compare anatomical form from imaging data, including Riemannian averaging [17, 10] and regression [11, 9, 28], applications in sparse representations [8, 27, 36], and deep learning [33, 29]. These techniques have largely been applied at the millimeter scale of human magnetic resonance imaging (MRI). Today, initiatives such as the Brain Research through Advancing Innovative Neurotechnologies (BRAIN), are leading to terabytes of neuroimaging data, typically acquired at subcellular resolution, publicly accessible through databases like the Brain Image Library (BIL) [6]. New mathematical and computational techniques are required to extract insight from the unprecedented scale of these neuroimaging datasets at micron resolution.

Multiplex error-robust fluorescence in situ hybridization (MERFISH) is one of several spatially resolved transcriptomic imaging technologies [32] that has been applied to characterize the transcriptomic profile and spatial location of cells within fixed brain tissues [5, 21, 31, 35]. Briefly, MERFISH uses massively multiplexed single-molecule FISH, error-robust barcoding, combinatorial labeling, and sequential imaging, to map the subcellular distributions of up to 10,000 RNA species (Fig. 1). Cells can be then segmented and the number of each RNA species

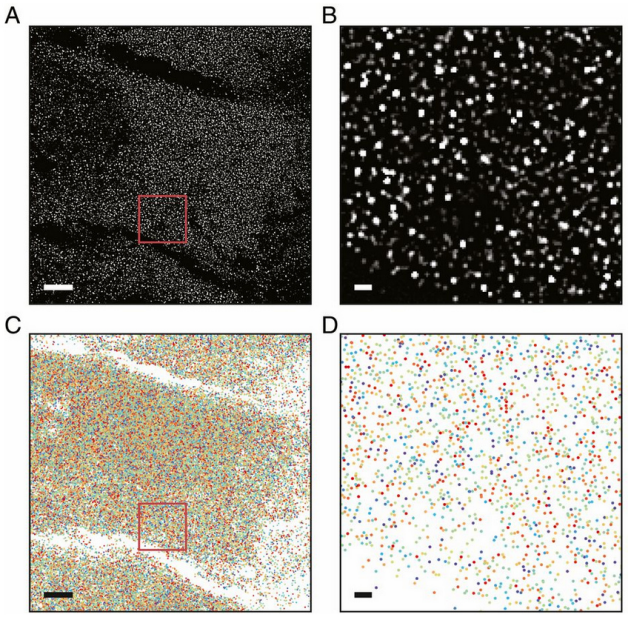

Figure 1. Example of MERFISH imaging of 10,050 genes in individual U-2 OS cells. (A) A high-pass-filtered, single-z slice image of a U-2 OS sample stained with encoding probes for a single imaging round. (Scale bar: 10 m.) (B) A zoomed-in image of the region marked with the red box in A. (Scale bar: 1 m.) (C) All identified RNA molecules (colored markers) detected from all imaged z slices in the region depicted in A. (Scale bar: 10 m.) (D) A zoomed-in image of all identified RNA molecules detected from all imaged z slices in the region marked with the red box in C. (Scale bar: 1 m.) In C and D, different colored dots mark distinct genes. Data from [31], images reproduced with permission.

within each cell quantified to achieve spatially resolved single-cell transcriptome profiling. Additional downstream single-cell clustering analysis may be applied to identify transcriptionally distinct cell-types and cell-states.

Our goal is to build a quantitative description of similarities and differences between these MERFISH datasets, in terms of their signal pattern and spatial distribution. In doing so we compute optimal spatial alignments in the form of diffeomorphic maps. These will be essential to 3D reconstruction of slices within a sample, alignment to well characterized atlases such as the Allen Institute Common Coordinate Framework [30], and for comparisons between samples acquired under different experimental conditions. Establishing a spatial alignment between images, and thus a distance between them, is natural at the 1mm macroscopic scale. For example, white matter and gray matter appear consistently in MRI scans of different subjects, and alignment of images can be computed by aligning the same tissue types. Even when images are acquired with different modalities, tissue types can be aligned based on their boundaries using approaches including mutual information [18, 22], local correlation [1], or image synthesis [13, 14, 26]. The challenge in extending these approaches to microscopic data is the lack of correspondence between particle type data in different images. For example, no two brains have the "same cells" and so aligning one to another at this scale is not as simple as aligning the image intensity of cells. This task requires an approach representing discrete cells and continuous tissues in a common framework.

Here we address this challenge through a multi scale solution, implementing methods described in [19]. We model MERFISH data using varifolds [4], which store the position and signal of particles using Dirac measures. We transition from fine to coarse scale using nonlinear descriptions of local statistical ensembles. And we model spatial patterns using flows of diffeomorphisms interacting at each scale, which extends the Riemannian setting of [2] to multiple scales.

2. Results

In this section we describe our MERFISH dataset and its representation at multiple scales using varifold measures. We follow with a review of the classic LDDMM method, and a description our diffeomorphic mapping approach. We then demonstrate its application to establishing a spatial correspondence between tissue sections.

2.1. MERFISH Data

The dataset we used was generated and made available publicly as part of the work described in [35]. To summarize, 7 to 8 week old mice were euthenized, and their brain was extracted and dissected into 3 millimeter cubes containing the entire preoptic region and surrounding nuclei. 12 slices, 10 microns thick and 50 microns apart were extracted and imaged with a high magnification, high-numerical aperture objective (Olympus, PlanApo 60/1.3 NA, silicon oil). For each slice 155 genes were imaged, cells were segmented, and counts per cell were converted to normalized z scores. Dimensionality was reduced with principal component analaysis, and clustering into cell types was performed with Jaccard-Louvain community-based detection with a bootstrap analysis to both identify stable clusters and select the optimal value of the nearest neighborhood size [16].

In Fig. 2 (top) we show a representation of 6443 detected cells, clustered into their 8 major types. The empty regions correspond to the ventricle (top) and ventral boundary of the brain (bottom). This sample consists of 5 slices, which are shown slightly smaller in the bottom two rows. As the slices move in the anterior to posterior direction, we can see the ventricle gradually disappear.

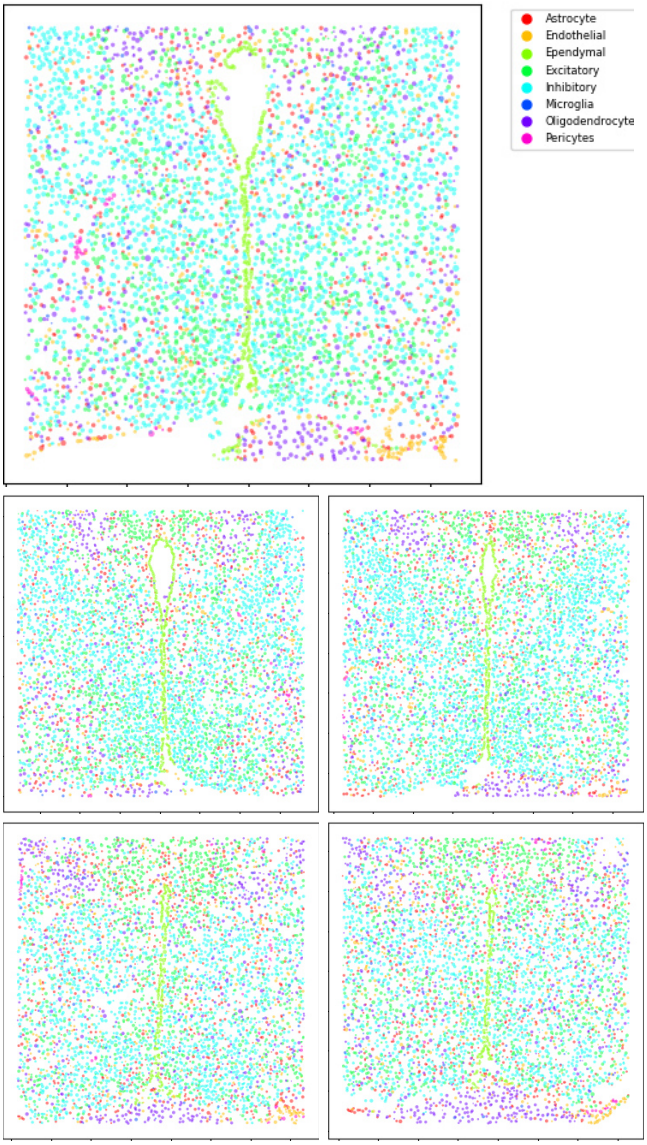

Figure 2. Top: One slice is shown near the preoptic hypothalamus. The 8 different major cell types are shown using a color key. In this figure only, the size of each dot corresponds to the size of the cell. Bottom: several other slices from this dataset are shown.

2.2. Multiscale varifold representation

In this work we focus on two spatial scales. At the fine scale (scale 0, indicated by a superscript 0) we have a set of cells with a spatial position, and a signal describing their type (a "one hot" encoded $M = 8$ dimensional vector). An example slice is shown on the top row of Fig. 2. We let each cell have position x_i^0, feature vector f_i^0, and weight $w_i^0 = 1$ for $i \in \{1, ..., N^0\}$ ($N^0 = 6443$ for this slice). We express this distribution as a weighted sum of Dirac measures:

$$\mu^0 = \sum_i w_i^0 \delta_{x_i^0} \otimes \delta_{f_i^0} \tag{1}$$

The first Dirac describes a measure over spatial position, and the second describes one over feature values.

At the coarse scale (scale 1, indicated by a superscript 1) we model tissues as mixtures of cell types. Spatial positions are described by a regular pixel grid at locations x_i^1 for $i \in 1, ..., N^1$ ($N^1 = 576$ for this slice, corresponding to a 24×24 pixel grid spaced at 92 microns). We transition between scales using a kernel, k, to identify locally weighted neighborhoods, and a set of summary statistics that describe these local ensembles. Here we used a 2D Gaussian kernel k. The weights are defined by

$$w_j^1 = \sum_i k(x_j^1, x_i^0) w_i^0 \ . \tag{2}$$

For each coarse scale particle, these weights are normalized to give a probability density, which is used to compute local statistics for new features,

$$p_j = \frac{1}{w_j^1} \sum_i k(x_j^1, x_i^0) w_i^0 \delta_{f_i^0} \ . \tag{3}$$

Note that for each j, this corresponds to a probability mass function over the 8 cell types.

We describe our data using two local statistics: a linear statistic (mean) and a nonlinear statistic (entropy) of the cell type distribution, giving 9 dimensions. This gives our varifold representation at coarse scale:

$$\mu^1 = \sum_j w_j^1 \delta_{x_j^1} \otimes \delta_{f_j^1} \ . \tag{4}$$

These coarse scale representations are illustrated in Fig. 3 for the same section as Fig. 2 (top). The left hand side shows local mean using the same color key as Fig. 2, and the right side shows local entropy. The color scale is set so that entropy of 0 bits is shown in black, and entropy of 3 bits (maximum possible for 8 cell types) is shown in bright red. Most of our data lies between 1.5 and 2.5 bits of entropy. Weights are shown using opacity, so that regions near the boundary or inside the ventricle appear transparent and are colored white.

In Fig. 4 we show the same fine and coarse scale representations for one slice in three other specimens.

2.3. Review of LDDMM

Image registration generally seeks to compute a smooth invertible transformation to deform one dataset to become similar to a second dataset. These transformations are maps between a subset of $\mathbb{R}^3$ to itself, $\varphi : X \subset \mathbb{R}^3 \to X$. Point

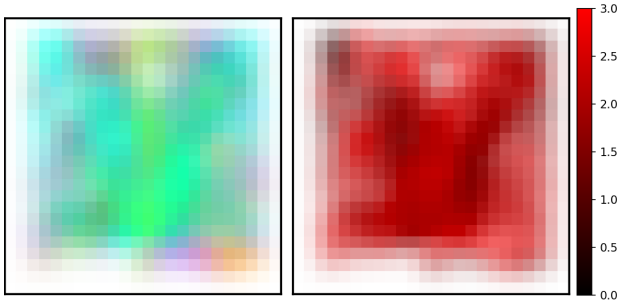

Figure 3. For the slice shown in Fig. 2 top, left shows local proportions of cell type, using the same color key. Right shows local entropy, with black 0 bits and red 3 bits. In both cases weights are mapped to opacity, such that regions appearing white have low weights.

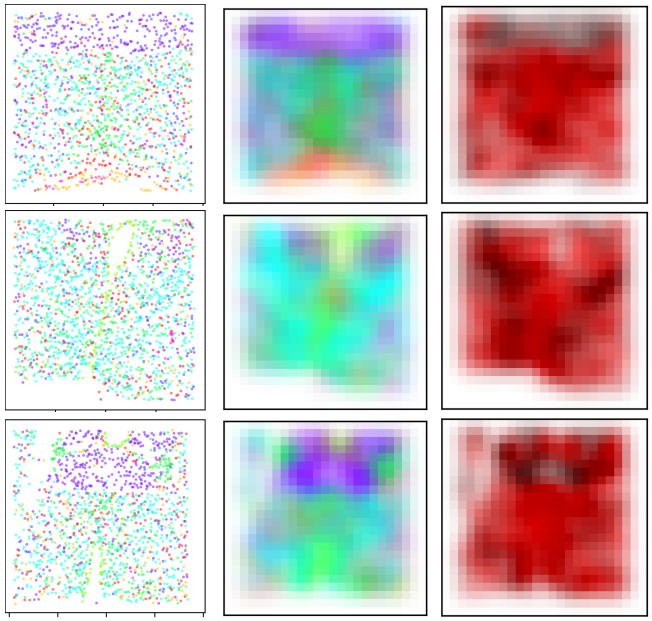

Figure 4. Fine and coarse scale representation of MERFISH data for 3 other specimens. Left column shows cell types at fine scale. Center column shows mean cell types at coarse scale, and right shows entropy in cell type distribution at coarse scale. Color is represented as in Fig. 2 and 3

.

based data (such as landmarks or discrete curves and surfaces) can be deformed by evaluating the map: $x_i \mapsto \varphi(x_i)$ directly, whereas imaging data can be deformed by composing images, $I : X \to \mathbb{R}$, with the inverse $I \mapsto I \circ \varphi^{-1}$.

In the LDDMM formalism for constructing diffeomorphic mappings between datasets, transformations are parameterized through a time varying velocity vector field, v_t for $t \in [0, 1]$. The transformation is generated by solving $\frac{d}{dt}\varphi_t = v_t(\varphi_t)$ with initial condition $\varphi_0 =$ identity. One can also consider points or images evolving dynamically under the flow v_t, with

$$\frac{d}{dt}x_i = v_t(x_i) \tag{5}$$

$$\frac{d}{dt}I = -DIv_t \tag{6}$$

for D placing components of partial derivatives across a row, and (6) being the optical flow equation.

This approach has a geometric interpretation, where v_t is a vector in the tangent space to the diffeomorphism group at φ_t. This tangent space is modeled as a reproducing kernel Hilbert space V. Relatively simple conditions on v_t can guarantee that φ be smooth and invertible [7]. Namely, an inner product is defined that penalizes quickly varying components through stationary highpass filter L, and the norm of v_t is used to regularize the deformation.

In the original implementation [2], optimal transformations were computed to align an image I to an image J (both functions from X to $\mathbb{R}$) by minimizing the objective function:

$$\frac{1}{2}\int_0^1 \|Lv_t\|^2_{L_2}dt + \frac{1}{2\sigma^2}\|I \circ \varphi_1^{-1} - J\|^2_{L_2}\,. \tag{7}$$

The first term imposes regularization through the norm squared in V, and the second corresponds to similarity through an L_2 norm. Optimal solutions are geodesic curves through the space of diffeomorphisms, and the regularization term is equal to the squared Riemannian distance between identity and φ_1. This problem is traditionally solved through gradient descent. Below we discuss our extension of this method to multi scale flows and multi scale datasets.

2.4. Multiscale diffeomorphic mapping

Given two multi scale representations of MERFISH datasets, a template and a target, we align one to another using geodesic trajectories in the space of diffeomorphisms. These diffeomorphisms are generated from flows (time varying velocity fields) at each scale: v_t^0 at fine scale and v_t^1 at coarse scale, for $t \in [0, 1]$.

These flows act on our varifold representation in two ways. First the position of particles is displaced by the velocity field:

$$\frac{d}{dt}x_i^0 = v^0(x_i^0) + v^1(x_i^0) \tag{8}$$

$$\frac{d}{dt}x_i^1 = v^1(x_i^1)\,. \tag{9}$$

Second, the weight of particles is modified by the velocity field's divergence.

$$\frac{d}{dt}\log(w_i^0) = \mathrm{div}[v^0](x_i^0) + \mathrm{div}[v^1](x_i^0) \tag{10}$$

$$\frac{d}{dt}\log(w_i^1) = \mathrm{div}[v^1](x_i^1) \tag{11}$$

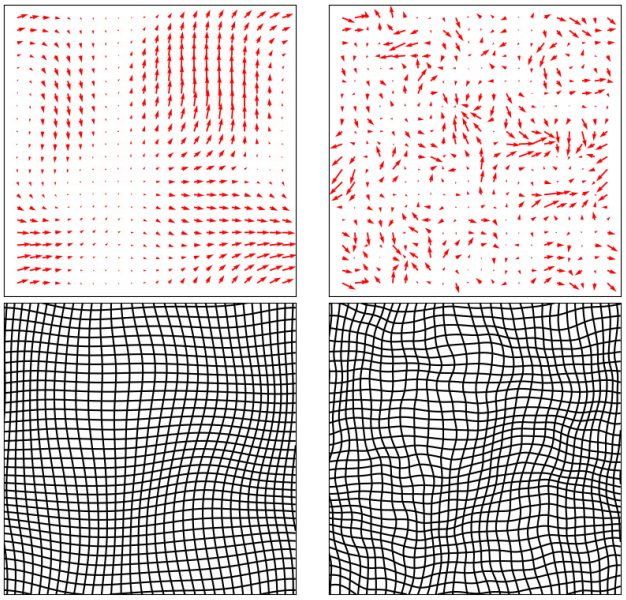

Figure 5. Top row: velocity vector fields at coarse (v^1, left) and fine (v^0, right) scale. Bottom row: v^1 is integrated to give φ^1 (left), and $v^0 + v^1$ is integrated to give φ^0 (right).

The feature values are not affected by this flow. Note that scales are coupled together, with v^0 interpreted as a refinement to v^1. These dynamic equations should be compared to their classic counterparts, with (8) and (9) directly comparable to (5), and (10) and (11) being comparable to (6).

We also generate dense diffeomorphisms sampled on a regular lattice at each scale (φ^0, φ^1):

$$\frac{d}{dt}\varphi^0 = v^0(\varphi^0) + v^1(\varphi^0) \tag{12}$$

$$\frac{d}{dt}\varphi^1 = v^1(\varphi^1)\,, \tag{13}$$

and their inverses:

$$\frac{d}{dt}(\varphi^0)^{-1} = -D[(\varphi^0)^{-1}](v^0 + v^1) \tag{14}$$

$$\frac{d}{dt}(\varphi^1)^{-1} = -D[(\varphi^1)^{-1}]v^1\,. \tag{15}$$

These are used for creating visualizations of deformed grids in Figs. 5,7,8. The black horizontal and vertical curves in these figures correspond to isocontours of the y and x components of φ^{-1} (respectively). The inverses involve the optical flow equation, which is computed using semi Lagrangian integration [7] (the method of characteristics). The idea of diffeomorphic flows at two different scales is illustrated in Fig. 5. Notice that the grid on the right maintains the same coarse scale trends as that on the left, but includes additional fine scale features.

The particle weights grow and shrink in proportion to the determinant of Jacobian of the diffeomorphism. This is illustrated in Fig. 6 and is equivalent to the equations (10) and (11).

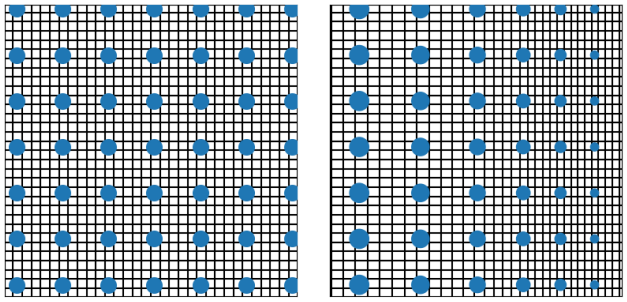

Figure 6. A set of particles sitting on an undeformed grid on the left, are transformed by a diffeomorphism represented by the deformed grid on the right. In regions where the grid is expansive (toward the $-x$ direction) the particle weights (represented as sizes) increase. In regions where the grid is compressive (toward the $+x$ direction) the particle weights decrease.

In our mapping method we minimize an objective function that penalizes the energy of the flows at each scale, ensuring the solution is a geodesic, as well as a matching cost at $t = 1$, which uses the varifold norm at each scale. The first term includes the regularization of [2] summed over each scale,

$$\text{Reg} = \int_0^1 \int \frac{1}{2\sigma_{R^0}^2}|L^0 v_t^0(x)|^2 + \frac{1}{2\sigma_{R^1}^2}|L^1 v_t^1(x)|^2 dx dt\,. \tag{16}$$

Here L^i is a differential operator of the form $(1 - a_i^2\Delta)^2$, with Δ the Laplacian, which is sufficient to ensure that any finite energy flow is smooth enough to generate a diffeomorphism [7]. The constants $\sigma_{R^0}^2, \sigma_{R^1}^2$ are user defined scalar weightings.

Data matching accuracy is evaluated at the endpoint of the flow ($t = 1$) using a varifold norm. This is an operator norm defined on a reproducing kernel Hilbert space with two kernels at each scale, one for spatial proximity (h_x^0,h_x^1) and one for features (h_f^0, h_f^1). We use Gaussians in both cases. At scale zero the norm of a varifold is defined by

$$\|\mu^0\|_0^2 = \sum_i \sum_{i'} w_i w_{i'} h_x^0(x_i - x_{i'}) h_f^0(f_i - f_{i'})\,, \tag{17}$$

and at scale 1 by

$$\|\mu^1\|_1^2 = \sum_j \sum_{j'} w_j w_{j'} h_x^1(x_j - x_{j'}) h_f^1(f_j - f_{j'})\,. \tag{18}$$

This gives us a total cost to minimize

$$\text{Cost} = \text{Reg} + \frac{1}{2\sigma_{M^0}^2}\|\mu_{t=1}^0 - \mu_{\text{target}}^0\|_0^2 + \frac{1}{2\sigma_{M^1}^2}\|\mu_{t=1}^1 - \mu_{\text{target}}^1\|_1^2\,. \tag{19}$$

Parameter	Equation	Fine	Coarse
Gaussian scaling k (μm)	(2),(3)	100.0	-
a (μm)	(16)	30	100
σ_R	(16)	5e3	1e3
σ_M	(19)	1.0	1.0
Gaussian position h_x (μm)	(17),(18)	50	200
Gaussian feature h_f	(17),(18)	1.0	1.0
Gradient descent step size	-	1e2	5e0
Optimization iterations	-	2000	-

Table 1. Parameter values used in our mapping algorithm. Quantities with units of length are expressed in microns. First and last line apply to both scales.

Note the negative of a varifold is found by negating its weights w.

Trajectories corresponding to minimizing solutions are constant speed geodesics in the space of multi-scale diffeomorphisms. Equations that characterize these solutions were derived in other work [19, 20].

2.5. Slice to slice alignment

We implement a minimization algorithm using automatic differentiation in pytorch. Velocity fields are discretized on fixed 35×34 grids with 75 micron spacing (note this does not use the "exact" reproducing kernel Hilbert space discretization described in [19]), and flows integrated with 5 timesteps using Euler's method. At fine scale, we decimated the number of cells by a factor of three so that our code would run an NVIDIA GeForce RTX 2080 Ti Rev. A (TU102) GPU with 11GB of memory. Other parameters used are described in Table 1.

In Fig. 7 we show the result of mapping one slice to its neighbor as a flow over time at coarse scale. From left to right the data is sampled at time $t \in \{0, 0.2, 0.4, 0.6, 0.8, 1.0\}$, with displayed grids rendered as isocontours of inverse diffeomorphism from (14) and (15). Notice that particle weights (represented as sizes) change in proportion to expansion or contraction of the grid. The color scale in the middle row indicates our entropy signal, with black 0 bits and red 3 bits.

In Fig. 8 we show the same at fine scale. Again it is clear that particle weights change significantly as well as position. The refined displacement, visualized as a grid shows a clear collapse of the ventricle to align data between the two slices. We note that there is a maximum displacement of approximately 140 microns, which corresponds to many times the size of a cell body. This shift accounts for deformations due to sectioning, but also due to changing anatomy as we progress from anterior to posterior. In either case this misalignment needs to be accounted for to make spatial comparisons between slices.

In Fig. 9 we show examples of mappings between different slices and different specimens, illustrating accuracy and generalizability. Some interesting features are revealed, such as the expansion of a small number of particles to fill in gaps as seen in the bottom row.

3. Conclusion

In this work we demonstrated the application of multi scale diffeomoprhic metric mapping to MERFISH datasets. This approach considered two scales, the cell-scale and the tissue-scale. We represented our data using varifolds, and diffeomorphisms using multi scale flows. We crossed from fine scale to coarse scale using locally weighted linear (mean) and nonlinear (entropy) statistics.

One limitation of with these reproducing kernel Hilbert space approaches is the quadratic complexity incurred in performing computations on the norm. This should be interpreted relative to hardware on which the images were acquired, which are currently limited to small fields of view due to long scanning times. Regardless, there have been approaches to address this in the field of computational anatomy, such as (non radially symmetric) kernels that involve interpolation to and from a fixed grid, and use of fast Fourier transforms [15].

Another limitation of this work is that while the framework permits as many scales as required, only two scales were used here. Future work will expand the number of scales that are mapped simultaneously toward the subcellular scale (as in Fig. 1), and toward more macroscopic scales. At the subcellular scale with millions of particles, overcoming quadratic complexity using fast kernels as mentioned above will be essential.

There have been several other approaches to mapping data at multiple scales. Some approaches have focused on the diffeomorphic transformation model, rather than representations of the data. Some authors have used regularization of diffeomorphic flows with velocity fields parameterized through kernels at different scales[23, 25]. These are summed into a single flow, but parameters can be separated by scale for later analysis. Other authors included concatenation of flows at different scales [3], and investigated the relationships to the previous approach. Other approaches have focused on the data model, for example using deep clustering [34] or wavelets [12] to extract features from high resolution data without considering multi scale flows. Relative to these techniques our approach has the advantage that it describes both point sets and images within a single framework, and considers the multi scale nature of both diffeomorphic mappings and data itself.

This work represents the first attempt to describe and quantify differences between MERFISH datasets by embedding their shape and signal in a Riemannian space. In future work these approaches will be extended towards several specific problems. These will include accurate 3D re-

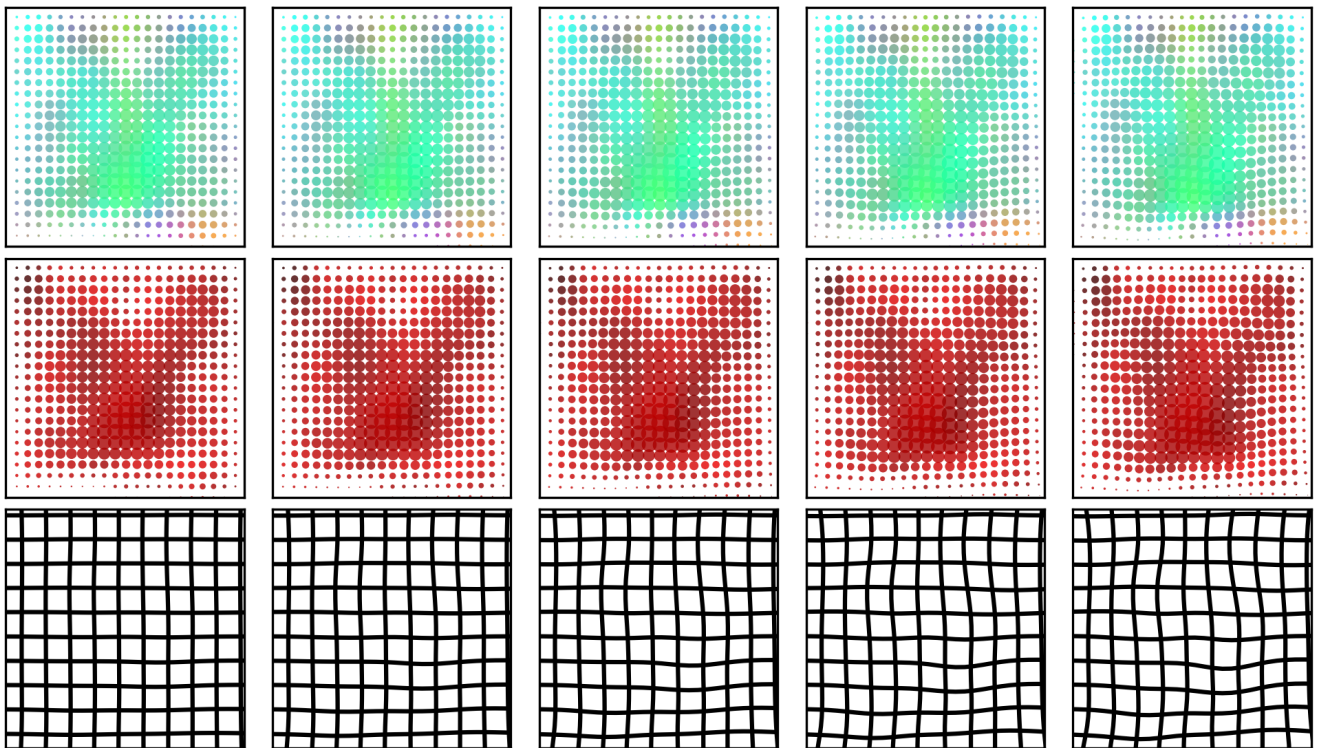

Figure 7. Slice to slice alignment results showing flows over time, from $t = 0$ (left) to $t = 1$ (right), at coarse spatial scale. The top row shows the deformation of mean cell type signal, with the same color key as Fig. 2. The second row shows the deformation of our entropy signal, with black 0 bits and red 3 bits. Particle weights are represented as sizes. The bottom rows show the diffeomorphism at this scale.

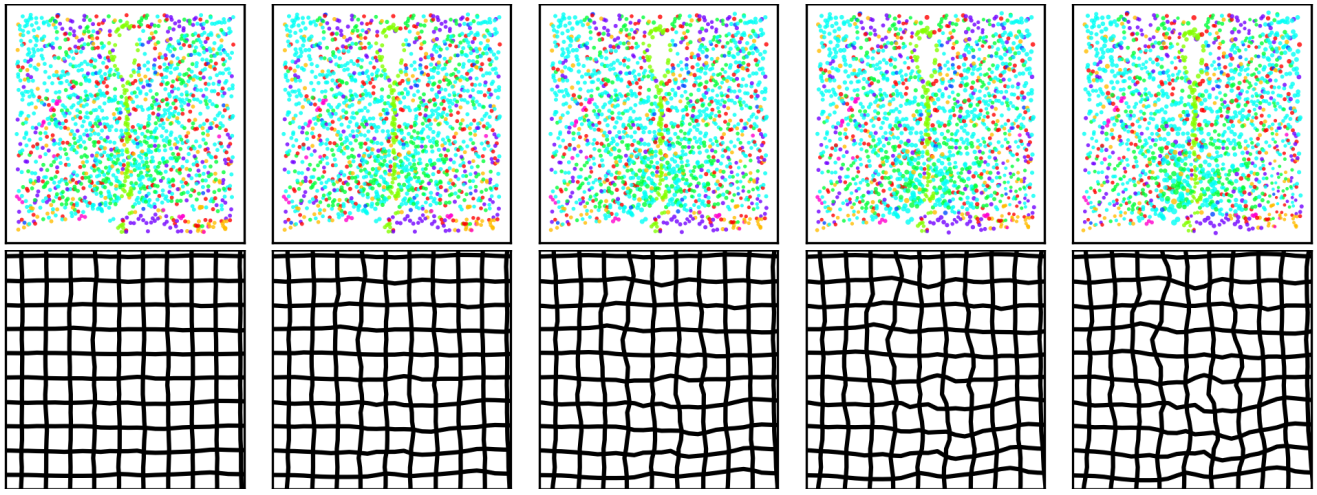

Figure 8. Slice to slice alignment results showing flows over time, from $t = 0$ (left) to $t = 1$ (right), at fine spatial scale. Particles shown using the same color key as Fig. 2. The top row shows the deformation of our cell type signal. Particle weights are represented as sizes. The bottom shows the diffeomorphism at this scale.

construction of serial sections, mapping to standard atlases, and hypotheses testing concerning spatial organization between populations of images taken under varying experimental conditions.

References

[1] Brian B Avants, Charles L Epstein, Murray Grossman, and James C Gee. Symmetric diffeomorphic image registration with cross-correlation: evaluating automated labeling of el-

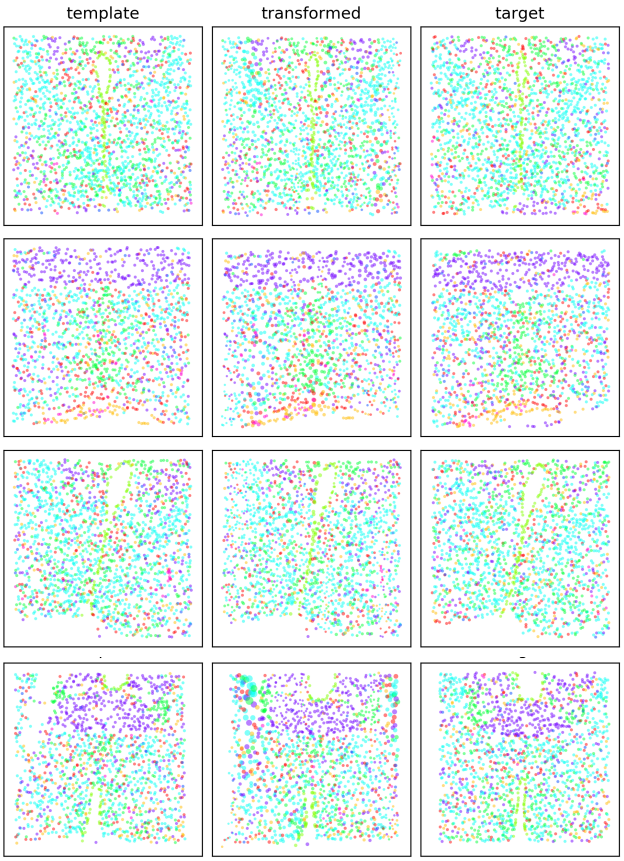

Figure 9. Slice to slice alignment for examples from four different datasets (rows). Particles shown using the same color key as Fig. 2. Left column: atlas, middle column: transformed atlas, right column: target.

derly and neurodegenerative brain. *Medical image analysis*, 12(1):26–41, 2008. 2

[2] M Faisal Beg, Michael I Miller, Alain Trouvé, and Laurent Younes. Computing large deformation metric mappings via geodesic flows of diffeomorphisms. *International journal of computer vision*, 61(2):139–157, 2005. 1, 2, 4, 5

[3] Martins Bruveris, Laurent Risser, and François-Xavier Vialard. Mixture of kernels and iterated semidirect product of diffeomorphisms groups. *Multiscale Modeling & Simulation*, 10(4):1344–1368, 2012. 6

[4] Nicolas Charon and Alain Trouvé. The varifold representation of nonoriented shapes for diffeomorphic registration. *SIAM Journal on Imaging Sciences*, 6(4):2547–2580, 2013. 2

[5] KH Chen, AN Boettiger, JR Moffitt, S Wang, and X Zhuang. Rna imaging. spatially resolved, highly multiplexed rna profiling in single cells. science 348, aaa6090, 2015. 1

[6] Sean Deitrich, Jacob Czech, Alexander Ropelewski, Arthur W Wetzel, Greg Hood, Derek Simmel, Marcel Bruchez, Simon C Watkins, and Alan M Watson. Applying irods to the brain image library. In *Proceedings of the Practice and Experience on Advanced Research Computing*, pages 1–4. 2018. 1

[7] Paul Dupuis, Ulf Grenander, and Michael I Miller. Variational problems on flows of diffeomorphisms for image matching. *Quarterly of applied mathematics*, pages 587–600, 1998. 4, 5

[8] Stanley Durrleman, Xavier Pennec, Alain Trouvé, and Nicholas Ayache. Sparse approximation of currents for statistics on curves and surfaces. In *International Conference on Medical Image Computing and Computer-Assisted Intervention*, pages 390–398. Springer, 2008. 1

[9] Stanley Durrleman, Xavier Pennec, Alain Trouvé, José Braga, Guido Gerig, and Nicholas Ayache. Toward a comprehensive framework for the spatiotemporal statistical analysis of longitudinal shape data. *International journal of computer vision*, 103(1):22–59, 2013. 1

[10] Stanley Durrleman, Marcel Prastawa, Julie R Korenberg, Sarang Joshi, Alain Trouvé, and Guido Gerig. Topology preserving atlas construction from shape data without correspondence using sparse parameters. In *International Conference on Medical Image Computing and Computer-Assisted Intervention*, pages 223–230. Springer, 2012. 1

[11] P Thomas Fletcher. Geodesic regression and the theory of least squares on riemannian manifolds. *International journal of computer vision*, 105(2):171–185, 2013. 1

[12] Daniel Fürth, Thomas Vaissière, Ourania Tzortzi, Yang Xuan, Antje Märtin, Iakovos Lazaridis, Giada Spigolon, Gilberto Fisone, Raju Tomer, Karl Deisseroth, et al. An interactive framework for whole-brain maps at cellular resolution. *Nature neuroscience*, 21(1):139–149, 2018. 6

[13] Juan Eugenio Iglesias, Ender Konukoglu, Darko Zikic, Ben Glocker, Koen Van Leemput, and Bruce Fischl. Is synthesizing mri contrast useful for inter-modality analysis? In *International Conference on Medical Image Computing and Computer-Assisted Intervention*, pages 631–638. Springer, 2013. 2

[14] Juan Eugenio Iglesias, Marc Modat, Loïc Peter, Allison Stevens, Roberto Annunziata, Tom Vercauteren, Ed Lein, Bruce Fischl, Sebastien Ourselin, Alzheimers Disease Neuroimaging Initiative, et al. Joint registration and synthesis using a probabilistic model for alignment of mri and histological sections. *Medical image analysis*, 50:127–144, 2018. 2

[15] Aastha Jain and Laurent Younes. A kernel class allowing for fast computations in shape spaces induced by diffeomorphisms. *Journal of Computational and Applied Mathematics*, 245:162–181, 2013. 6

[16] Jacob H Levine, Erin F Simonds, Sean C Bendall, Kara L Davis, D Amir El-ad, Michelle D Tadmor, Oren Litvin, Harris G Fienberg, Astraea Jager, Eli R Zunder, et al. Data-driven phenotypic dissection of aml reveals progenitor-like cells that correlate with prognosis. *Cell*, 162(1):184–197, 2015. 2

[17] Jun Ma, Michael I Miller, Alain Trouvé, and Laurent Younes. Bayesian template estimation in computational anatomy. *NeuroImage*, 42(1):252–261, 2008. 1

[18] David Mattes, David R Haynor, Hubert Vesselle, Thomas K Lewellen, and William Eubank. Pet-ct image registration in

the chest using free-form deformations. *IEEE transactions on medical imaging*, 22(1):120–128, 2003. 2

[19] Michael I Miller, Daniel J Tward, and Alain Trouvé. Coarse-to-fine hamiltonian dynamics of hierarchical flows in computational anatomy. In *Proceedings of the IEEE/CVF Conference on Computer Vision and Pattern Recognition Workshops*, pages 860–861, 2020. 2, 6

[20] M I Miller, D J Tward, and A Trouve. Hierarchical computational anatomy: Unifying the molecular to tissue continuum via measure representations of the brain. *bioRxiv*, 2021. 6

[21] Jeffrey R Moffitt, Dhananjay Bambah-Mukku, Stephen W Eichhorn, Eric Vaughn, Karthik Shekhar, Julio D Perez, Nimrod D Rubinstein, Junjie Hao, Aviv Regev, Catherine Dulac, et al. Molecular, spatial, and functional single-cell profiling of the hypothalamic preoptic region. *Science*, 362(6416), 2018. 1

[22] Josien PW Pluim, JB Antoine Maintz, and Max A Viergever. Mutual-information-based registration of medical images: a survey. *IEEE transactions on medical imaging*, 22(8):986–1004, 2003. 2

[23] Laurent Risser, François-Xavier Vialard, Robin Wolz, Maria Murgasova, Darryl D Holm, and Daniel Rueckert. Simultaneous multi-scale registration using large deformation diffeomorphic metric mapping. *IEEE transactions on medical imaging*, 30(10):1746–1759, 2011. 6

[24] C Schmitz and PR Hof. Design-based stereology in neuroscience. *Neuroscience*, 130(4):813–831, 2005. 1

[25] Stefan Sommer, Mads Nielsen, François Lauze, and Xavier Pennec. A multi-scale kernel bundle for lddmm: towards sparse deformation description across space and scales. In *Biennial International Conference on Information Processing in Medical Imaging*, pages 624–635. Springer, 2011. 6

[26] Daniel Tward, Timothy Brown, Yusuke Kageyama, Jaymin Patel, Zhipeng Hou, Susumu Mori, Marilyn Albert, Juan Troncoso, and Michael Miller. Diffeomorphic registration with intensity transformation and missing data: Application to 3d digital pathology of alzheimer's disease. *Frontiers in neuroscience*, 14:52, 2020. 2

[27] Daniel Tward, Michael Miller, Alain Trouve, and Laurent Younes. Parametric surface diffeomorphometry for low dimensional embeddings of dense segmentations and imagery. *IEEE transactions on pattern analysis and machine intelligence*, 39(6):1195–1208, 2016. 1

[28] Daniel J Tward, Chelsea S Sicat, Timothy Brown, Arnold Bakker, Michela Gallagher, Marilyn Albert, Michael Miller, Alzheimer's Disease Neuroimaging Initiative, et al. Entorhinal and transentorhinal atrophy in mild cognitive impairment using longitudinal diffeomorphometry. *Alzheimer's & Dementia: Diagnosis, Assessment & Disease Monitoring*, 9:41–50, 2017. 1

[29] Jian Wang and Miaomiao Zhang. Deepflash: An efficient network for learning-based medical image registration. In *Proceedings of the IEEE/CVF conference on computer vision and pattern recognition*, pages 4444–4452, 2020. 1

[30] Quanxin Wang, Song-Lin Ding, Yang Li, Josh Royall, David Feng, Phil Lesnar, Nile Graddis, Maitham Naeemi, Benjamin Facer, Anh Ho, et al. The allen mouse brain common coordinate framework: a 3d reference atlas. *Cell*, 181(4):936–953, 2020. 2

[31] Chenglong Xia, Jean Fan, George Emanuel, Junjie Hao, and Xiaowei Zhuang. Spatial transcriptome profiling by merfish reveals subcellular rna compartmentalization and cell cycle-dependent gene expression. *Proceedings of the National Academy of Sciences*, 116(39):19490–19499, 2019. 1, 2

[32] A Xiaowei. Method of the year 2020: spatially resolved transcriptomics. *Nature Methods*, 18(1), 2021. 1

[33] Xiao Yang, Roland Kwitt, Martin Styner, and Marc Niethammer. Quicksilver: Fast predictive image registration–a deep learning approach. *NeuroImage*, 158:378–396, 2017. 1

[34] Paul A Yushkevich, Mónica Muñoz López, Maria Mercedes Iñiguez de Onzoño Martin, Ranjit Ittyerah, Sydney Lim, Sadhana Ravikumar, Madigan L Bedard, Stephen Pickup, Weixia Liu, Jiancong Wang, et al. 3d mapping of neurofibrillary tangle burden in the human medial temporal lobe. *bioRxiv*, 2021. 6

[35] Meng Zhang, Stephen W Eichhorn, Brian Zingg, Zizhen Yao, Hongkui Zeng, Hongwei Dong, and Xiaowei Zhuang. Molecular, spatial and projection diversity of neurons in primary motor cortex revealed by in situ single-cell transcriptomics. *bioRxiv*, 2020. 1, 2

[36] Miaomiao Zhang, William M Wells III, and Polina Golland. Probabilistic modeling of anatomical variability using a low dimensional parameterization of diffeomorphisms. *Medical image analysis*, 41:55–62, 2017. 1